Methane separation from diluted mixtures by fixed bed adsorption using MOFs: model validation and parametric studies

David Ursueguía, Eva Díaz, Aurelio Vega, Salvador Ordóñez[a]

[a]Catalysis, Reactors and Control Research Group (CRC), Department of Chemical and Environmental Engineering, University of Oviedo, 33006, Spain
e-mail: sordonez@uniovi.es, Tel: +34 985 103 437; Fax: + 34 985 103 434

ABSTRACT

Adsorption of methane from diluted methane/nitrogen mixtures in a fixed bed reactor was experimentally studied and modelled in this work. Three different Metal-Organic Frameworks (MOFs), Basolite C300, F300 and A100 were considered for this purpose, the adsorption bed being operated at 298 K, 0.1 MPa, and an inlet methane concentration of 2%. Methane adsorption capacities decrease in the order: Basolite C300 (0.078 mmol/g) > Basolite F300 (0.040 mmol/g) > Basolite A100 (0.028 mmol/g). In addition, a mechanistic model based on the numerical solution of an heterogeneous one-dimensional model considering axial dispersion has been used for modelling these adsorption results.

Proposed model provides a reasonable fitting of the experimental fixed bed results ($R^2 > 0.9$), using internal diffusion and axial dispersion as fitting parameters. Variation of these parameters can be explained in terms of adsorbent morphological features. Proposed model has been successfully extended to other methane adsorption processes reported in the literature, as well as to thermal desorption of methane from MOF-containing fixed bed reactors. The experimentally validated model has been used to predict the effect of main operation parameters on the performance of the MOF-based fixed beds for methane adsorption.

Keywords: CH_4/N_2 separation; fixed bed; breakthrough curve; Comsol model; VAM

1. INTRODUCTION

Coal mines release methane to the atmosphere in the preconditioning stage previous to the coal bed exploitation, as well as during coal mining operations (coal mine methane) and also after the shafts closure [1]. It is estimated that only in the US, coal mines liberate about 112 Tg CO_2 eq. annually, of which less than 14% is recovered and used [2]. The remaining methane is vented to the atmosphere, representing a loss of valuable energy source. More than 90% of these coal mine methane emissions are believed to be from underground mines, of which about 70-80% is emitted in very diluted form (typically less than 1% of methane) through the mine ventilation air, which is known as ventilation air methane (VAM) [3]. It must be also considered that these emissions remain even after the coal mine closure. This desorption process may continue for many years after closure but at a rapidly declining rate and, where a mine is flooded, can resume when flooded mine workings are dewatered [4]. As a consequence, this methane constitutes an important hazard, thus exploitation or mitigation of methane from closed underground coal mines will minimize potential hazards, reduce emissions and potentially create revenue [5].

The main features of the VAM emissions are their low methane concentration (0.1-1%) and high flow rates (up to 600 m^3/s), a direct upgrading of these streams being strongly hindered [6]. The most feasible and environmentally friendly solution is to pre-concentrate methane in these streams. The main components of the streams are nitrogen, carbon dioxide, oxygen, water and methane [7], being needed to separate methane from the other components [8]. Nitrogen is the main component in the mixture (~ 78%), and it is also the most similar in molecular size to methane (3.64 and 3.80 Å [9], respectively). In addition, both molecules present a null dipole moment. These features make the separation CH_4/N_2 the most complicated to carry out.

Fakhroleslam and Fatemi [10], compare methane purification techniques (pressure swing adsorption, vacuum swing adsorption and temperature swing adsorption) using SAPO-34-core-shell as adsorbent, concluding that temperature swing adsorption (TSA) reaches the best purification efficiency. In fact, TSA is usually recommended in purification processes from lean mixtures (< 2% of the interesting compound) [11]. Concerning the adsorbent, among different materials tested for this separation: inorganic materials [12-15], carbonaceous adsorbents [16], and metal-organic frameworks (MOFs) [17-20], the latter are considered the most promising behavior in the methane separation from a diluted stream. Although several works are focused on the adsorbent selection and the study of the adsorption equilibrium [19, 20], the study of the adsorption dynamics is not so developed, in spite of its larger importance in the design of adsorption-based processes.

If the adsorption of other lean gases is considered, several studies on the modelling of breakthrough curves for CO_2 [21], and H_2S [22] gas adsorption have been published. Several

previous works deal with the CO_2 adsorption from a methane stream [8], and even, Delgado et al. [23] published data on methane adsorption from methane/nitrogen mixtures where methane concentrations vary from 8 to 70%. Although some of these works applied mathematical models to predict the adsorption fixed bed dynamics in terms of partial differential equations [23], with its consequent complexity; it is still required the development of mechanistic and rigorous models for simulating the saturation and operation of the adsorption bed in several conditions. Concerning modelling approach for selective separation from diluted streams [24, 25], most of the works apply Gran Canonical Monte-Carlo (GCMC) method for the simulations, which allows simulating the adsorptive behavior of the materials at certain conditions and with different structural variations in the adsorbents [26, 27], but they are not suitable for providing rigorous simulation of fixed bed adsorption processes at operating conditions.

With this background, the challenge addressed in this work is focused on two underdeveloped fields: the methane/nitrogen separation from streams with low methane concentration, as well as the rigorous modelling of the breakthrough curves of the adsorption process. Fixed-bed adsorption process was numerically modeled using an axially dispersed plug flow model with non-linear isotherms based on the linear driving force (LDF) approximation. A parametric study shows the effect of some operational parameters (particle size, inlet flow and adsorbent bed parameters) on intrinsic parameters (axial dispersion and mass transfer resistance) and then, on the final performance. Simulated data were validated with the experimental results of methane adsorption present in low-concentrated currents from nitrogen in a fixed-bed operated at lab scale, using as adsorbents three of the most used commercial MOFs (Basolite C300, F300 and A100).

2. EXPERIMENTAL SECTION

2.1. Materials

Basolite F300 [Iron 1,3,5-benzenetricarboxylate, $C_9H_3FeO_6$], Basolite C300 [Copper 1,3,5-benzenetricarboxylate, $Cu_3(C_9H_3O_6)_2$] and Basolite A100 [Aluminium terephthalate, $C_8H_5AlO_5$], all supplied by *Badische Anilin- und Soda-Fabrik* (BASF), were used as adsorbents without further purification. All the gases used in this work, methane (CH_4), nitrogen (N_2) and helium (He), had purity higher than 99.995% mol, and were supplied by Air Liquide. Table 1 provides a morphological description of the three adsorbent materials.

Table 1. Morphological specifications of the materials according to the manufacturer

Parameter	***Basolite C300***	***Basolite F300***	***Basolite A100***
Density (kg/m^3)	350	160-350	400
Pore size (Å)	11/10/4 [1]	18/5.5/8.6 [2]	8.5 [3]
Specific surface (m^2/g)	1500-2100	1300-1600	1100-1500
Particle size (μm)	16 (D50)	5 [4]	32 (D50)

[1] Reference [28]; [2] Reference [29]; [3] Reference [30]; [4] Reference [31]

2.2. Apparatus and experimental procedure

Adsorption experiments were performed by passing gas mixtures through a column packed with the adsorbent. This packed bed consisted of a stainless steel tube of 520 mm length and 6.4 mm of internal diameter. Adsorbents (0.5 g) with particle sizes between 5 and 32 μm were placed in the middle of the tube and in contact with a K-type thermocouple which gave the actual temperature values throughout the experiments. The length of the adsorbent bed is 45 mm for Basolite C300 and F300, and 39 mm for Basolite A100, respectively. These values confirmed the plug flow regime restrictions [32]: $D/d_p > 10$ and $L/d_p > 50$, being D the adsorbent bed diameter, L the bed length and d_p the particle size. Pressure drop along the fixed bed is about 0.06 MPa for all cases. The remaining void column volume was filled with glass beads (1 mm). The flowrate of each gas was controlled with mass flow controllers (Bronkhorst), being the total flow 50 mL/min at 0.1 MPa and 298 K.

Prior to the adsorption tests, the surface of the adsorbent is cleaned and degasified by a pure helium flow (50 mL/min) at 373 K until no other gases were detected in the analyzer. Then, adsorption experiments were conducted at 298 K, and the gases were mixed before entering to the fixed bed. The effluent gases were analyzed by mass spectrometry in a previously calibrated Pfeiffer Vacuum apparatus. On the other hand, desorption experiments were conducted at 333 K using nitrogen as carrier gas (1 mL/min and 0.1 MPa) through the fixed-bed previously saturated in the problem mixture. As in the adsorption stage, the outlet is analyzed by the mass spectrometer.

In addition, concentrations of both gases (methane and nitrogen) between 0 and 5% in helium were introduced into the fixed bed at the same conditions (298 K, 0.1 MPa) with the aim of obtaining the methane and nitrogen adsorption isotherms. The same experience was performed at 333 K in the desorption stage for different inlet methane concentrations (0 – 5%) for saturation, thus obtaining the desorption constants.

Breakthrough theoretical curves, and subsequent parametric variations, were obtained from a differential equations (PDE) solver (Comsol Multiphysics® Version 5.4.) that solves the theoretical model equations numerically. The accuracy of the predicted models was measured comparing the R-squared method of experimental and theoretical results.

3. MATHEMATICAL MODEL

3.1. Breakthrough curve model

Fixed bed adsorption/desorption experiments were modelled using a dynamic heterogeneous one-dimensional model. Gas and solid phases were independently considered, which allows observing differences in the concentration of both phases. Isothermal conditions, negligible radial dispersion and changes in fluid velocity, as well as spherical and homogeneous in size and density adsorbent particles (bed void fraction constant) are assumed. The isothermal character is assumed considering both the low adsorption enthalpies (~ 20 kJ/mol) [33, 34], and the high adsorbate dilution. This dilution, and the high D/d_p and L/d_p ratios, allow considering the flow through the bed as turbulent.

The differential mass balance for the adsorbate in the gas phase includes accumulation, convection flow, axial dispersion and the interphase transfer or adsorption rate. In the solid phase, accumulation and the interphase transfer terms are included, as summarized in Table 2.

Table 2. Terms of the model differential equations.

	Accumul.	Convection	Dispersion	Interphase transfer	Reaction
Gas mass balance	$\frac{\partial C_i}{\partial t} =$	$-\frac{u_0}{\varepsilon_b}\frac{\partial C_i}{\partial z}$	$+D_e\frac{\partial^2 C_i}{\partial z^2}$	$-\rho_b\left(\frac{1-\varepsilon_b}{\varepsilon_b}\right)\frac{\partial q_i}{\partial t}$	
Solid mass balance	$\frac{\partial W_i}{\partial t} =$			$+\frac{\partial q_i}{\partial t}$	

Interphase mass transfer is considered by the dependent variable q_i, which corresponds with the *i* component concentration in the solid phase, and correlates this transport with an equilibrium gradient. This last assumption is valid, because of the absence of chemical reaction in both phases as well as the negligibility of physical transport effects on the solid phase.

Equilibrium isotherms were determined in a previous work [35]. A simple Langmuir model was used to adjust it (Eq. 1). Q_{mi} and K_{Li} are the parameters of the simple Langmuir model for each gas.

$$W_{ieq} = \frac{Q_{mi} \cdot K_{Li} \cdot C_i}{1 + K_{Li} \cdot C_i} \qquad \text{(Eq. 1)}$$

In order to solve the differential equations, Danckwerts boundary conditions (Table 3) were considered as currently proposed for fixed beds [36]. These conditions are taken for the both ends of the fixed bed (z = 0 and z = L_b).

Table 3. Boundary conditions.

	$z = 0$	$z = L_b$
Gas mass balance	$(C)_{0^-} = (C)_{0^+} - \frac{D_e}{v_0}\left(\frac{\partial C}{\partial z}\right)_{0^+}$	$\left(\frac{\partial C}{\partial z}\right)_{z=L_b} = 0$
Solid mass balance	$\left(\frac{\partial W}{\partial z}\right)_{z=0^+} = 0$	$\left(\frac{\partial W}{\partial z}\right)_{z=L_b} = 0$

3.2. Physical and transport properties

Gas phase physical properties (density, viscosity, heat capacity and thermal conductivity) are assumed to be the corresponding to the diluent (nitrogen or helium), due to the low methane concentration (max. 5%). Solid physical properties are known or estimated from the specifications of the manufacturer.

One of the most important transport properties is axial dispersion (D_e). This property is calculated from Edwards and Richardson's correlation (Eq. 2). This correlation is based on the Péclet number (Pe), defined as the relation between convection and diffusion in a mass or heat transport process, in which the particle size is the characteristic length [21]. On the other hand, D_m is the molecular diffusion, calculated by the Fuller-Schettler-Gridding correlation (Eq. 3) [37]. The surface velocity (u_0) is easily calculated from the inlet flow and the cross-section of the fixed bed. The bed porosity is approximated to 0.4 according to Theuerkauf et al. [38], supposing randomly packed bed of spheres.

$$D_e = 0.73 \cdot D_m + \frac{0.5 \cdot u_0 \cdot d_p}{1 + 9.49 \cdot \frac{D_m}{u_0 \cdot d_p}} \quad \text{(Eq. 2)}$$

$$D_m = \frac{0.001 \cdot T^{1.75} \cdot \left(\frac{1}{M_A} + \frac{1}{M_B}\right)}{P \cdot \left(V_A^{\frac{1}{3}} + V_B^{\frac{1}{3}}\right)^2} \quad \text{(Eq. 3)}$$

In the adsorption process, the interphase mass transport, $dq_i/dt = k_L \cdot (W_{ieq} - W_i)$, controls the mass transfer step in the process and it is described in terms of crystal radius (r_c), effective diffusivity (D_i) and equilibrium parameters, according to Eq. 4 [39].

$$\frac{1}{k_L} = \frac{r_p \cdot W_0}{3k_f \cdot C_0} + \frac{{r_p}^2 \cdot W_0}{15 \cdot \varepsilon_p \cdot D_p \cdot C_0} + \frac{{r_c}^2}{15 \cdot D_i} \quad \text{(Eq. 4)}$$

In Eq. 4, k_L considers all the mass-transfer resistances for the transport of the adsorbate from the bulk gas phase to the adsorbent surface. The first term is related to the external fluid film resistance, which depends linearly on the adsorbent particle radius (r_p), and it is appreciable when the adsorption rate is limited by the flow of the gas to the surface. The k_f parameter is the film mass transfer coefficient and W_0 is the solid phase adsorbate concentration in equilibrium with the inlet gas-phase concentration (C_0). The second term is related to the diffusion in macropores as the controlling step, which is important when most of the pores in the adsorbent are macropores, or when its size (more than 50 nm) limits the entrance of adsorbate molecules; D_p being the macropore diffusivity. The last term is important when the adsorption is controlled by the diffusion in micropores, as taking place when most of the pores are microporous (up to 2 nm). In this case, D_i is the micropore diffusivity. The great crystallinity of these materials at its original form, makes it possible to assimilate crystal and particle radius. Due to the high microporous character of MOFs and the small size of their pores, the final equation for the mass transport is (Eq. 5):

$$\frac{dq_i}{dt} = 15 \cdot \frac{4D_i}{{d_p}^2} \cdot \left(W_{ieq} - W_i\right) \quad \text{(Eq. 5)}$$

Where W_{ieq} is the solid-gas equilibrium concentration that can be calculated through the adsorption isotherm of the material. Thus, there is an intraparticle resistance at micropores with a surface diffusion mechanism.

In summary, the final equations for the model are summarized in Table 4.

Table 4. Final equations for the proposed model for fixed bed adsorption.

	Accumul.	Convection	Dispersion	Interphase transfer
Gas mass balance	$\frac{\partial C_i}{\partial t} =$	$-\frac{u_0}{\varepsilon_b}\frac{\partial C_i}{\partial z}$	$+D_e\frac{\partial^2 C_i}{\partial z^2}$	$-15\cdot\frac{4\cdot\rho_b\cdot(1-\varepsilon_b)}{\varepsilon_b\cdot {d_p}^2}\cdot D_i\cdot\left(W_{ieq}-W_i\right)$
Solid mass balance	$\frac{\partial W_i}{\partial t} =$			$+15\cdot\frac{4D_i}{{d_p}^2}\cdot\left(W_{ieq}-W_i\right)$

4. RESULTS AND DISCUSSION

4.2. Fixed bed adsorption

4.2.1. Single adsorbate adsorption

Experimental breakthrough adsorption curves of 5% methane and nitrogen in helium over the three Basolites tested in this work are shown in Fig. 1, whereas Table 5 includes the parameters used in Comsol Multiphysics implementation to perform the theoretical simulations. The microporous diffusivity term (D_i) is used as the fit parameter to the experimental data due to its difficult experimental calculation reported by other authors [21, 40]. Basolite C300 presents the highest adsorption capacity for both adsorbates (Table 6) and also, more remarkable for methane, in agreement with the CH_4/N_2 adsorption isotherms [35].

Table 5. Parameters used in Comsol simulation to solve the differential equations for adsorbate/helium mixtures. A multifrontal massively parallel sparse direct solver (MUMPS) has been implemented as model solver in the program.

METHANE						
Material	u_0 (m/s)	ε_b	D_e (m^2/s)	ρ_b (kg/m^3)	d_p (m)	K_{Hi} (mol/kg)
C300	0.026	0.4	$4.6\cdot10^{-5}$	350	$16\cdot10^{-6}$	4.53
F300	0.026	0.4	$4.6\cdot10^{-5}$	350	$5\cdot10^{-6}$	3.40
A100	0.026	0.4	$4.6\cdot10^{-5}$	400	$32\cdot10^{-6}$	4.08

NITROGEN						
Material	u_0 (m/s)	ε_b	D_e (m^2/s)	ρ_b (kg/m^3)	d_p (m)	K_{Hi} (mol/kg)
C300	0.026	0.4	$5.1 \cdot 10^{-5}$	350	$16 \cdot 10^{-6}$	2.88
F300	0.026	0.4	$5.1 \cdot 10^{-5}$	350	$5 \cdot 10^{-6}$	2.64
A100	0.026	0.4	$5.1 \cdot 10^{-5}$	400	$32 \cdot 10^{-6}$	2.23

The best fitting to the model was obtained for the Basolite A100 (R^2 = 0.99 for both methane and nitrogen), followed by Basolite C300 (0.96 and 0.98) and Basolite F300 (0.94 and 0.98). The estimated values of the micropore diffusivity (D_i) were $8.1 \cdot 10^{-10}$, $7.2 \cdot 10^{-10}$ and $5.1 \cdot 10^{-11}$ m^2/s for C300, F300 and A100, respectively in case of methane, and $8.2 \cdot 10^{-9}$, $7.3 \cdot 10^{-9}$ and $4.2 \cdot 10^{-11}$ m^2/s, respectively in case of nitrogen. These values are similar to those presented by Bárcia et al. [41] for MOF-508b, obtained also by fitting the experimental responses, and also to the micropores diffusion obtained experimentally from kinetic studies on Mg-MOF-74 by Bao et al. [42]. Therefore, with a single fit parameter, it is possible to obtain a good fitting to experimental results but with some deviations in the slopes, especially for C300 and F300. Observed deviations are due to consider the same axial dispersion coefficient for all materials, based on the low-sensitive correlation used (Eq. 2). Thus, considering D_e another fitting parameter (keeping the previous D_i values), a reduction of axial dispersion coefficients is observed for Basolite F300 and C300: $9.1 \cdot 10^{-6}$ and $5.2 \cdot 10^{-6}$ m^2/s, respectively for methane, and $2.1 \cdot 10^{-5}$ and $9.1 \cdot 10^{-6}$ m^2/s, respectively for nitrogen. Modifications in D_e and D_i parameters do not affect the total adsorption capacity of each material, which remains constant for both simulations. The area behind the breakthrough curve is the same for each material and gas in each case. Simulations led to higher regression coefficients in all cases, Fig 1. Likewise, Basolite A100 keeps the same values. Axial dispersion coefficient is higher for Basolite A100 due to the highest particle diameter, already considered in the correlation (Eq. 2). Therefore, the correlation seems to be more applicable for materials with high densities and particle sizes.

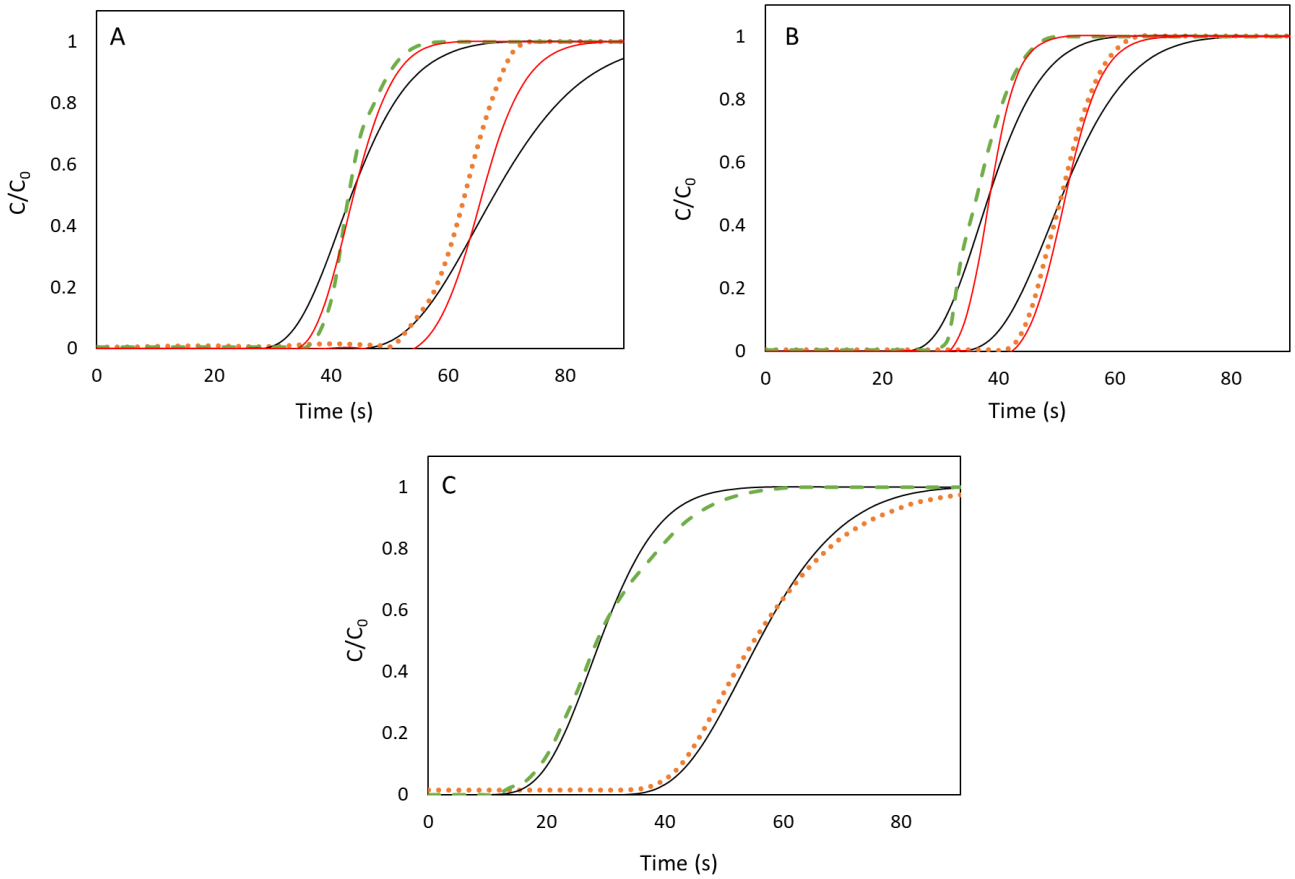

Figure 1. Breakthrough curves of Basolite C300 (A), Basolite F300 (B) and Basolite A100 (C) (5 % of methane (orange dotted line) and nitrogen (green discontinuous line) in helium) 298 K, 0.1 MPa. Black solid lines correspond to fitting only considering D_i as fitting parameter whereas colored solid lines correspond to fit both D_i and D_e.

Experimental results show that Basolite C300 presents the maximum adsorption capacity of the three studied materials, both for nitrogen and methane (Table 6). This fact corresponds with the order in specific surface of the materials, which is especially important at high pressures, at which there is usually a linear relationship between both parameters [43]. In those cases, the gas is distributed on the surfaces in relation to the available space. In addition, Basolite C300 also presents a high concentration of open metal sites in its structure (31.5% of copper), compared to 21.2% of iron for Basolite F300 and 12.9% of aluminium in Basolite A100, being remarkable that the trend is the same than in the previous case [44]. This may be one of the reasons why these materials clearly present greater adsorption capabilities than other common adsorbents, such as carbon nanotubes [45] or zeolite 4A [14], at similar temperatures and partial pressures. In any case, the two previous parameters cannot explain certain deviations of the theoretical behavior. For example, Basolite A100 presents higher adsorption capacity for methane than Basolite F300,

despite its specific surfaces are very different, as well as its metal content. This fact suggests that mass transfer effects play a key role in the fixed bed dynamics.

Table 6. Adsorption capacity (W_{ieq}) of CH_4 and N_2 (5%) in He at 0.1 MPa of total pressure and 298 K.

Adsorbent	Methane uptake (mmol/g)	Nitrogen uptake (mmol/g)
Basolite C300	0.23	0.14
Basolite F300	0.17	0.13
Basolite A100	0.20	0.11

At this point, the resulting fitting parameter (D_i) is higher for nitrogen. Nitrogen presents smaller molecular size than methane (3.65 and 3.82 Å, respectively), thus it is easier to penetrate in the structure of the adsorbent. However, for Basolite A100, the presence of methane induces the existence of a large-pore configuration that makes D_i higher for methane, promoting the penetration [46], so it could be the reason of the higher adsorption capacity than Basolite F300. It could also explain the highest adsorption values in case of Basolite C300 despite its smaller pore size, but it has higher micropore volume, 0.56 cm^3/g versus 0.30 and 0.35 cm^3/g for F300 and A100, respectively, which also eases the accessibility (higher D_i) [35]. Finally, physical properties could increase the diffusional effects and also the slope of the breakthrough curve. For example, in case of Basolite A100, for the same adsorbent weight, due to its higher density, the bed length is reduced. This fact, add to the largest particle size among the three materials, enhances the diffusional effects [32], thus a higher curve inclination is observed. The latter concept highlights the importance of axial dispersion (D_e), as it was shown in Fig. 1.

The developed model was applied to experimental data obtained from the literature [23], observing the goodness of the fitting, Fig. 2. Delgado et al. [23] used silicalite for the designing of a pressure swing adsorption process. The bed length and diameter (0.163 and 0.016 m, respectively) are close to the experimental device used in the present work. Langmuir isotherm was also used by the authors in order to obtain equilibrium data at 0.09 MPa and 298 K for an initial methane concentration of 14% in helium. Applying the Comsol generated model to the experimental data of the work, the simulated breakthrough time is really similar to the experimental data, but the slope of the curve is higher, indicating a higher simulated dispersion. The value of D_i is $9.1 \cdot 10^{-10}$ m^2/s, higher than for methane adsorption on MOFs, which involves the easiness to penetrate into the structure, as it could be expected from the higher pore size and particle macroporosity. The slight deviation of the simulation respect to the slope of the

experimental data is corrected in a second simulation, by modifying the value of D_i up to $1.5 \cdot 10^{-9}$ m^2/s, which indicates a higher mass transfer rate than the considered initially.

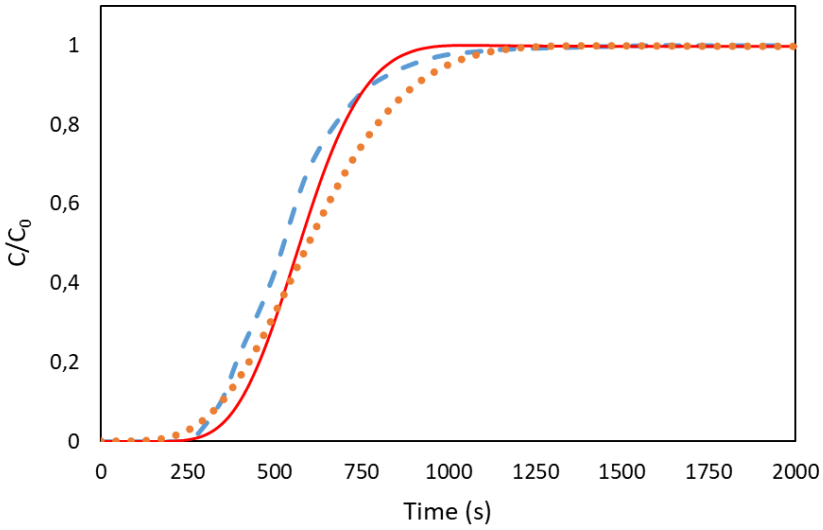

Figure 2. Application of the generated mathematical model to other material and process (silicalite for methane/helium (14/86) at 0.09 MPa and 298 K [23]). This work's model [orange dotted line (first simulation) and red continous line (second simulation)], other author's data (blue discontinuous line).

Thus, developed model is suitable for a wide range of materials and conditions. In addition, the mass transfer, and, therefore, the morphology and the structure of the materials are the most important parameters for a suitable operation.

4.2.1. CH_4/N_2 adsorption

Fig. 3 shows the methane breakthrough curve for the 2% of methane/nitrogen feed, at 298 K and 0.1 MPa, showing a situation close to the VAM stream. Table 7 includes the parameters used in Comsol Multiphysics implementation to perform the simulations. In this case, adsorption isotherms also consider the presence of nitrogen, which is also an adsorbable gas, since the adsorption of both gases occurs simultaneously [35], (Eq. 2). Model fitting correlation (R^2) are: 0.99, 0.91 and 0.97 for Basolite C300, F300 and A100, respectively. D_i is used as the only fitting parameter.

At these conditions, differences in the methane adsorption capacities are more marked than for methane diluted in a noble gas: Basolite C300 (0.078 mmol/g) > Basolite F300 (0.040 mmol/g) > Basolite A100 (0.028 mmol/g). In fact, the adsorption capacity of Basolite C300 is about 48.7% higher than for Basolite F300 in the CH_4/N_2 mixture, whereas only a 26.1% higher for experiences

in inert diluent, as well as 64.1 versus 13% in Basolite A100 case. Thus, the largest Lewis acid concentration in Basolite C300 due to the metal open sites could favor the selective methane adsorption in presence of nitrogen, due to its higher polarizability [47].

Table 7. Parameters used in Comsol simulation to solve the differential equations for methane/nitrogen mixtures.

METHANE							
Material	v_0 (m/s)	ε_b	D_e (m^2/s)	ρ_b (kg/m^3)	d_p (m)	K_{Li} (kg/mol)	Q_{mi} (mol/kg)
C300	0.026	0.4	$1.6 \cdot 10^{-5}$	350	$16 \cdot 10^{-6}$	0.106	5.11
F300	0.026	0.4	$1.6 \cdot 10^{-5}$	350	$5 \cdot 10^{-6}$	0.018	7.71
A100	0.026	0.4	$1.6 \cdot 10^{-5}$	400	$32 \cdot 10^{-6}$	0.118	1.59

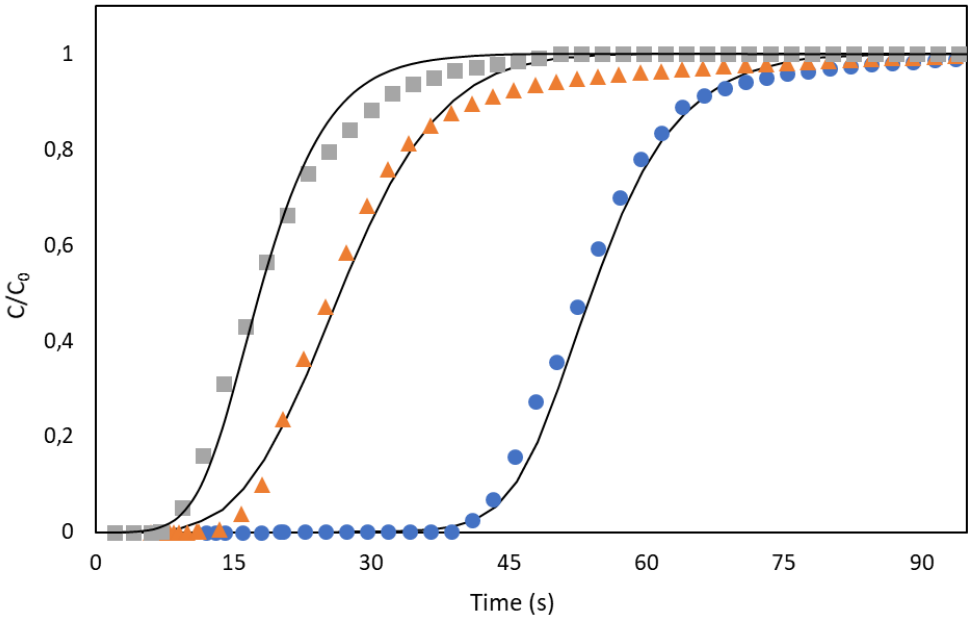

Figure 3. Methane breakthrough curves for low-grade methane adsorption (2% of methane in nitrogen, 50 mL/min) 298 K, 0.1 MPa. Basolite C300 (Blue filled circles), Basolite F300 (Orange filled triangles) and Basolite A100 (Grey filled squares). Black lines symbolize the fit to the breakthrough curve model.

The obtained D_i values are: $1.2 \cdot 10^{-12}$, $2 \cdot 10^{-13}$ and $5 \cdot 10^{-12}$ m^2/s, respectively for C300, F300 and A100. Basolite A100 presents the highest axial dispersion coefficient in the methane/nitrogen mixture. Although the large-pore configuration of this material also enhances the nitrogen

adsorption, its preference for methane adsorption (ratio of 2.12 for pure CH_4/N_2 adsorption at 298 K [35]) causes a substantial improvement in methane accessibility. The improved access to open metal sites favors especially methane adsorption, since methane polarizability is higher, thus its adsorption on acid centers [47] would increase the selectivity of the process. Similarly, Couck et al. [48] have observed the favored adsorption of CO_2 in the CO_2/CH_4 separation.

Concerning Basolite C300, Deniz et al. [49] have demonstrated the existence of two main adsorption sites in the structure. However, at low pressures, only the site near to the metal centers is active. This site allows the CH_4/N_2 separation (ratio of 2.04 for pure CH_4/N_2 adsorption at 298 K [35]). This adsorption ratio increases until reaching its maximum at 313 K (2.15), which points out a chemical specificity of the open Cu site [35]. Contrary, the same authors [49] have defined for Basolite F300 a single interaction area for all pressure range, with a CH_4/N_2 ratio = 2.11.

4.3. Fixed bed desorption

Proposed model will be only useful if it is also able to predict the behavior of the fixed bed during the regeneration. In order to obtain a concentrated methane stream at the outlet of the bed, a desorption curve for Basolite C300 is shown in Fig. 4. Modelling of desorption operation after the adsorption one, just considers the operation conditions and the adsorbate transference from the solid to the gas phase. Desorption begins just after the low-grade methane (2%) adsorption stage. Once the bed access valves are closed, the temperature increase begins at 10 K/min until desorption temperature, 333 K, which is maintained for 2 hours. Then, valves are opened and 1 mL/min of nitrogen as drag gas is introduced at 0.1 MPa of total pressure. Nitrogen gas flow was selected as low as possible in order to get a methane concentrated stream. On the other hand, desorption temperature (333 K) was selected as a compromise between the thermal stability of the materials and the operational costs. In addition, the optimum temperature for CO_2 desorption from MOFs is about 373 K [50], so, for methane, a lower temperature could be enough due to its slightly weaker interaction. At these operation conditions, the maximum methane concentration obtained is 2.94% in nitrogen, so, a maximum concentration increment of 46.7% was achieved.

Simulation properties were calculated by analogy to adsorption, whereas desorption constant was determined from in situ experiences. Simulation parameters are summarized in Table 8, obtaining a good fit to the experimental data ($R^2 = 0.98$). It is remarkable the increase in the D_i fit value ($9.1 \cdot 10^{-9}$ m^2/s), in comparison to adsorption one, which could be related to the temperature increment [51-53]. In addition, axial dispersion (D_e) is slightly oversized by the correlation, as expected when working at lower flow rates.

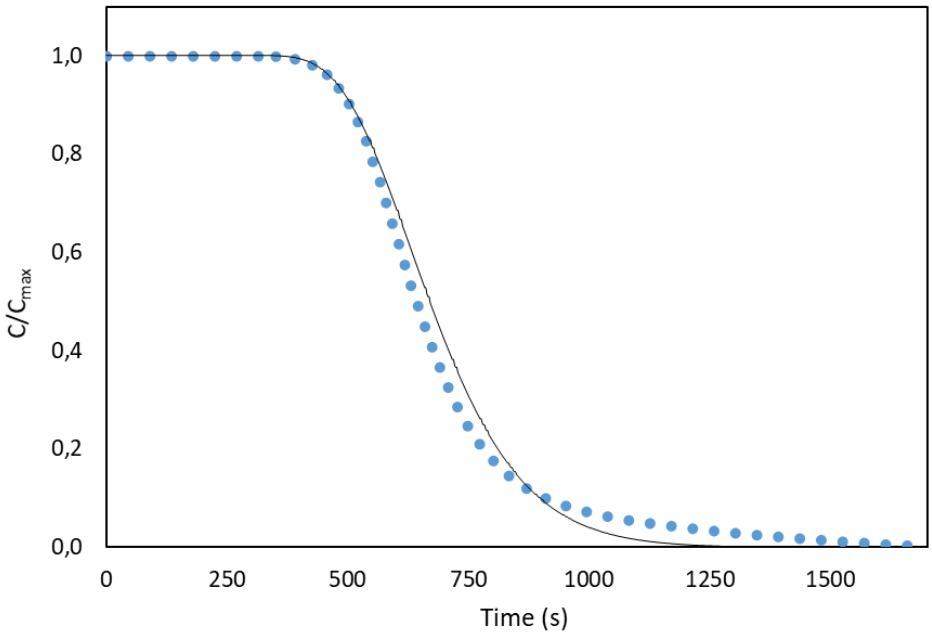

Figure 4. Methane desorption curve after low-grade methane adsorption (333 K, 1 mL/min of nitrogen and 0.1 MPa). Experimental data (blue filled circles). Black line symbolizes the fit to the desorption model generated. $C_{max,CH4}$ = 2.94%.

Table 8. Desorption process data to solve differential equations

METHANE						
Material	v_0 (m/s)	ε_b	D_e (m^2/s)	ρ_b (kg/m^3)	d_p (m)	K_{Hi} (mol/kg)
Basolite C300	0.00052	0.4	$1.60 \cdot 10^{-6}$	350	$16 \cdot 10^{-6}$	0.92

4.4. Parametric study of the effect of design parameters on the adsorption behavior

Once checked the suitability of the mathematical model to the experimental results, the effect of varying operational parameters was studied in order to identify those parameters influencing adsorption behavior at larger extent. This parametric study was performed for Basolite C300 material. The study is divided into the different modified parameters.

Increase in fixed bed length (1 to 8 cm), keeping porosity and density of the adsorbent, enhances the final total methane adsorbed and, hence, the breakthrough time. The equilibrium remains constant without variations in temperature or pressure (Fig. 5). However, the pressure drop increases also with the bed length, reaching more than 0.1 MPa from 7 cm according to estimations from mechanical balance. Variations in the shape of the breakthrough curve, which

losses its typical ‘S’ shape [54], were already reported after fixed bed length changes for very complex adsorbate molecules, far from the methane and nitrogen structures.

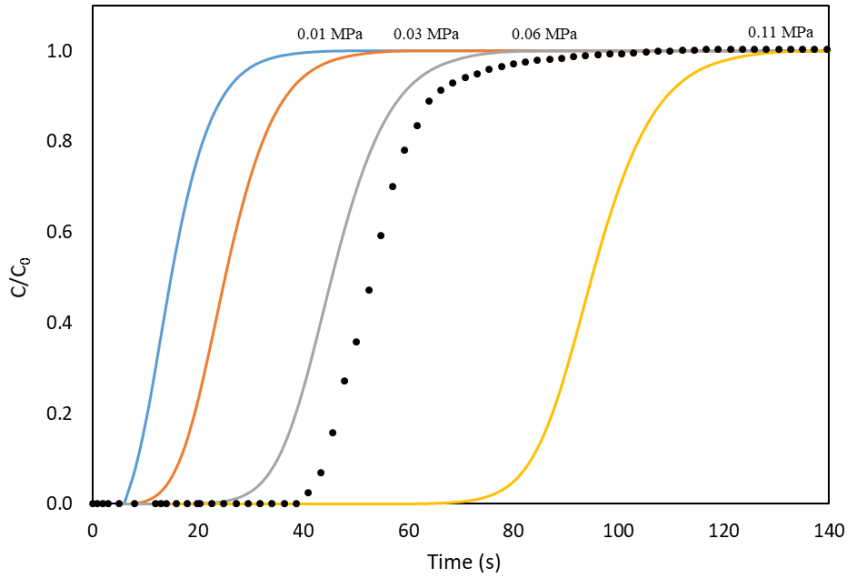

Figure 5. Methane breakthrough curves for low-grade methane adsorption onto Basolite C300 (2% of methane in nitrogen) 298 K and 1 bar for different bed lengths: 1 cm (Blue), 2 cm (Orange), 4 cm (Grey) and 8 cm (Yellow). Total pressure drops are provided near to each curve. Black dotted line corresponds to the experimental breakthrough curve.

Variations in the inlet flow (10 to 80 mL/min) influences directly the surface velocity in the fixed bed, and hence, the axial dispersion (Figure 6). According to Eq. 2, the smallest particle size has a great influence on the axial dispersion value, so the variations of inlet flow are irrelevant. Likewise, the pressure drop in the bed increases with the inlet flow, being reduced the breakthrough time [55]. Final methane adsorption capacity does not vary since the equilibrium is unaltered. However, if the surface velocity hinders the appropriate gas-solid contact, a controlling step in the kinetics of the process would generate a premature breakthrough.

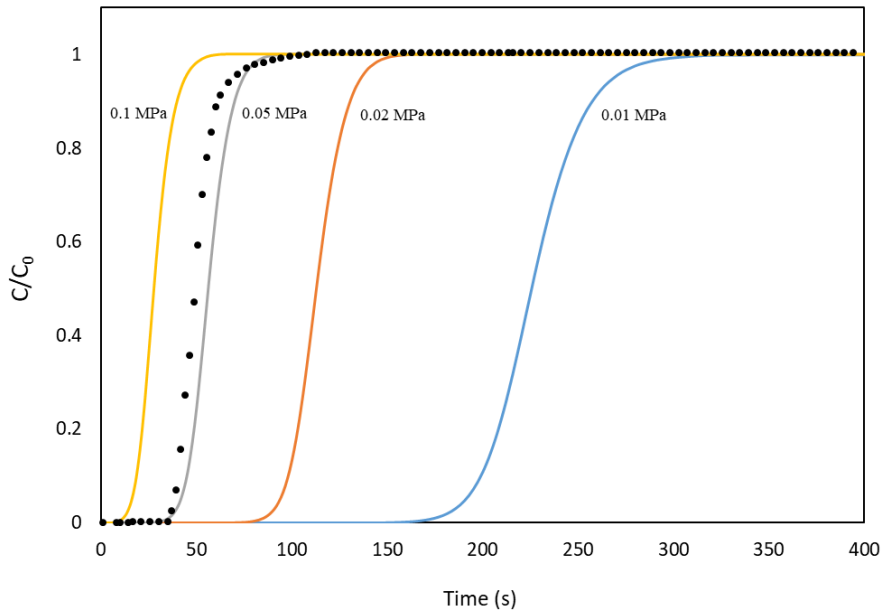

Figure 6. Methane breakthrough curves for low-grade methane adsorption onto Basolite C300 (2% of methane in nitrogen) 298 K and 1 bar for different inlet flows: 10 mL/min (Blue), 20 mL/min (Orange), 40 mL/min (Grey) and 80 mL/min (Yellow). Total pressure drops are indicated near to each curve. Black dotted line corresponds to the experimental breakthrough curve.

Adsorbent morphological parameters, specially particle size, undoubtedly affect the pressure drop and the adsorption yield. An increment in the particle size increases the mass transfer resistance, thus influences the adsorption rate due to the reduction of the interphase mass transfer coefficient (Eq. 5). In addition, particle size has a direct influence above void fraction, which is an important parameter in the mechanical balance to the pressure drop calculations. Fig. 7 shows several simulations for changes in particle size (10 to 40 µm). Structure and internal parameters of the adsorbents are considered the same as in previous case, but other changes are taken into account, like bed density or bed length.

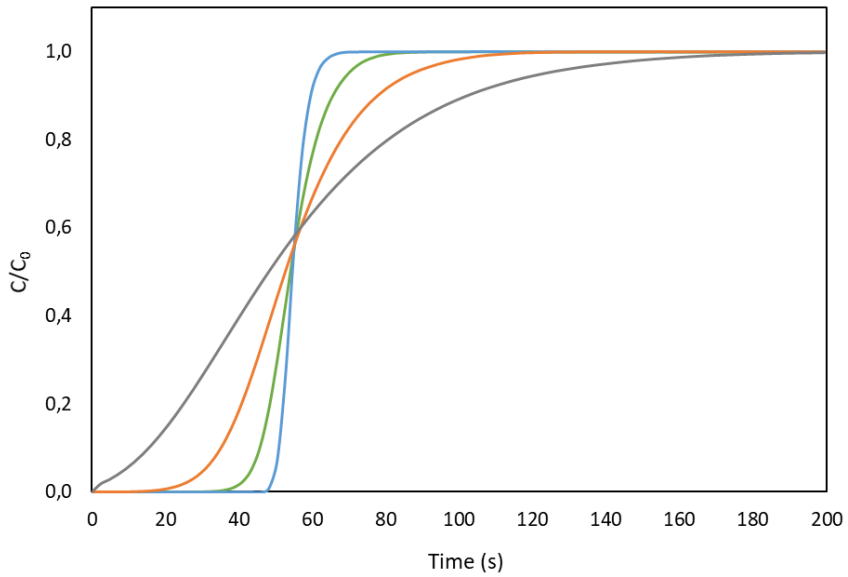

Figure 7. Methane breakthrough curves for low-grade methane adsorption onto Basolite C300 (2% of methane in nitrogen) 298 K and 1 bar for different particle sizes: 10 µm (Blue), 16 µm (Green), 25 µm (Orange) and 40 µm (Grey).

For the smallest particle sizes, it is observed the highest breakthrough time, since the smallest particles have a shorter diffusion path, thus allowing the adsorbate to penetrate deeper into the adsorbent particle more quickly [56]. On the other hand, high variations in the slopes of the curves are associated with the effect on axial dispersion of particle size increments, in addition to lower breakthrough times. Calculated pressure drops for each case by a mechanical balance are 0.16, 0.06, 0.02 and 0.01 MPa in increasing particle size order, respectively. This makes the pressure drop the limiting step in particle size effect, making necessary to reach a compromise between breakthrough time and pressure drop.

Variations in previous parameters involve intrinsic changes in the process, such as axial dispersion and mass transfer coefficient. From Eq. 2, axial dispersion depends mainly on the particle diameter, the surface velocity and the molecular diffusion. An increment of any of these parameters results in axial dispersion enhancement. Likewise, the molecular diffusion increases with the temperature and decreases with pressure. Figure 8 shows the variation of the breakthrough curve with variations in axial dispersion ($5 \cdot 10^{-6}$ to $5 \cdot 10^{-4}$ m^2/s), with unaltered curves for axial dispersion values lower than $5 \cdot 10^{-6}$ m^2/s. Thus, adsorbate transport by axial dispersion is negligible in comparison to the convective transport [57]. Axial dispersion reaches the presented limiting value ($5 \cdot 10^{-4}$ m^2/s) at 70 m/s of inlet velocity, 2 cm of particle diameter, 0.25 bar of total pressure or 1300 K of temperature, independently. All that values are unreachable for a device of these characteristics, so axial dispersion is not a limiting parameter.

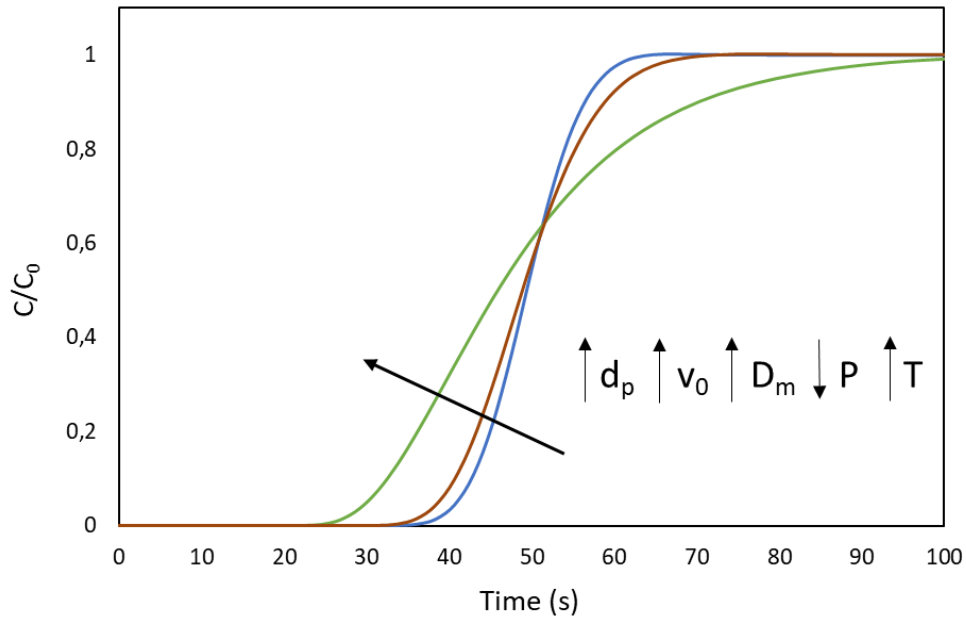

Figure 8. Methane breakthrough curves for low-grade methane adsorption onto Basolite C300 (2% of methane in nitrogen) 298 K and 0.1 MPa for different axial dispersions: $5 \cdot 10^{-4}$ m^2/s (Green), $5 \cdot 10^{-5}$ m^2/s (Brown) and $5 \cdot 10^{-6}$ m^2/s (Blue).

On the other hand, the mass transfer coefficient depends mainly on the microporous diffusivity and the particle size. Fig. 9 shows the influence on the breakthrough curve of the microporous diffusivity (10^{-12} to 10^{-9} m^2/s). For diffusivities lower than 10^{-12} m^2/s, it is lost the typical shape due to the low intrapore diffusivity, so the more difficult penetration of the adsorbates in the structure of the adsorbent. In general, the larger the diffusivity, the smaller the diffusion resistance within the micropores, resulting in a steeper breakthrough curve. In addition, a higher particle size and a lower pore size difficult the molecules crossing through the pores, and, therefore, the interaction with open metal sites.

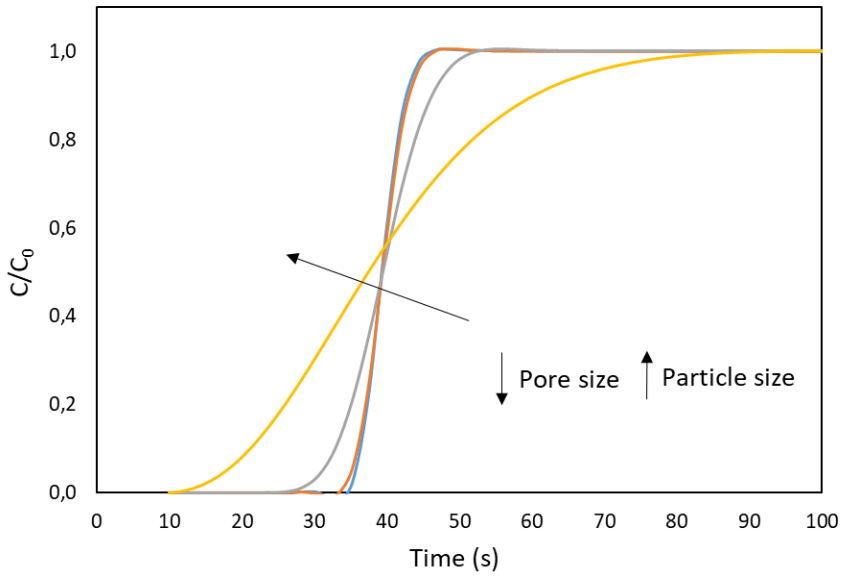

Figure 9. Methane breakthrough curves for low-grade methane adsorption onto Basolite C300 (2% of methane in nitrogen) 298 K and 0.1 MPa for different micropores diffusivities: 10^{-12} m^2/s (Yellow), 10^{-11} m^2/s (Grey), 10^{-10} m^2/s (Orange) and 10^{-9} m^2/s (Blue).

5. CONCLUSIONS

Materials with well-defined structures such as Metal-Organic Frameworks are potential candidates to be used in gas separation operations. The presence of metal active adsorption sites, its high specific surfaces and the regular pore sizes, in addition to the existence of commercial available types, represent a starting point for industrial-scale production and use. A mathematical model that allows simulating a gas separation at low concentrations has been generated validating it with the laboratory low-methane concentration adsorption experiments on three Basolites (C300, F300 and A100). The model has achieved good adjustments both for the three Basolites (R^2 = 0.99, 0.91 and 0.97, respectively), and for bibliographic data. Basolite C300 presented the best performance for recovering methane: good selectivity (CH_4/N_2 = 1.64) and high uptake capacity (0.078 mmol/g), despite its low concentration (2% CH_4), and even higher than some of the most common adsorbents, such as zeolite 4A and carbon nanotubes. These conditions allow obtaining an increment of 46.7% respect to inlet methane concentration after an adequate desorption stage. In addition, the known structure of the materials allowed making parametric studies about several parameters (bed length, inlet flow and particle size) and study its influence on others (axial dispersion and mass transfer coefficient). The model allows variating a vast number of parameters in order to study the effect on the breakthrough curve, which is of high importance for future scale-ups.

6. ACKNOWLEDGMENTS

This work was supported by the Research Fund for Coal and Steel of the European Union (contract UE-17-RFCS216-METHENERGY PLUS). David Ursueguía acknowledges the Spanish Ministry of Education for the PhD grant that supports his research.

7. REFERENCES

[1] D. Zhong, W. Wang, Z. Zou, Y. Lu, J. Yan, K. Ding, Investigation on methane recovery from low-concentration coal mine gas by tetra-n-butyl ammonium chloride semiclathrate hydrate formation, Appl. Energ. 227 (2018) 686-693. https://doi.org/10.1016/j.apenergy.2017.08.069.

[2] United States Environmental Protection Agency, Inventory of US greenhouse gas emissions and sinks: 1990-2012, EPA 430-R-14-003. Washington, DC: US Environmental Protection Agency; 2014.

[3] UNECE, Best practice guidance for effective methane drainage and use in coal mines, ECE Energy Series No. 47 Cap. 1 Pag. 27, 2016.

[4] UNECE, Best practice guidance for effective methane drainage and use in coal mines, ECE Energy Series No. 47 Cap. 6 Pag. 65, 2016.

[5] A. Duda, A. Krzemien, Forecast of methane emission from closed underground coal mines exploited by longwall mining – A case study of Anna coal mine, J. Sustain. Mining 17 (2018) 184-194. https://doi.org/10.1016/j.jsm.2018.06.004.

[6] P. Tremain, A. Maddocks, B. Moghtaderi, Stone dust looping for ventilation air methane abatement: a 1 m^3/s pilot-scale study, Energ. Fuels 33 (2019) 12568-12577. https://doi.org/10.1021/acs.energyfuels.9b02932.

[7] J. Fernández, P. Marín, F. Díez, S. Ordóñez, Combustion of coal mine ventilation air methane in a regenerative combustor with integrated adsorption: Reactor design and optimization, Appl. Therm. Eng. 102 (2016) 167-175. https://doi.org/10.1016/j.applthermaleng.2016.03.171.

[8] D. Qu, Y. Yang, Z. Qian, P. Li, J. Yu, A. Ribeiro, A. Rodrigues, Enrichment of low-grade methane gas from nitrogen mixture by VPSA with CO_2 displacement process: modeling and experiment, Chem. Eng. J. 380 (2020) 122509. https://doi.org/10.1016/j.cej.2019.122509.

[9] X. Hou, S. Liu, Y. Zhu, Y. Yang, Experimental and theoretical investigation on sorption kinetics and hysteresis of nitrogen, methane, and carbon dioxide in coals, Fuel 268 (2020) 117349. https://doi.org/10.1016/j.fuel.2020.117349.

[10] M. Fakhroleslam, S. Fatemi, Comparative simulation study of PSA, VSA, and TSA processes for purification of methane from CO2 via SAPO-34 core-shell adsorbent, Sep. Sci. Technol. 51 (2016) 2326-2338. https://doi.org/10.1080/01496395.2016.1210640.

[11] Yang RT. Adsorbents: fundamentals and applications. 1st ed. John Wiley & Sons; 2003.

[12] P. Li, H. Tezel, Adsorption separation of N2, O2, CO2 and CH4 gases by β-Zeolite, Micropor. Mesopor. Mat. 98 (2007) 94-101. https://doi.org/10.1016/j.micromeso.2006.08.016.

[13] X. Xu, X. Zhao, L. Sun, X. Liu, Adsorption separation of carbon dioxide, methane and nitrogen on monoethanol amine modified β-zeolite, J. Nat. Gas Chem. 18 (2009) 167-172. https://doi.org/10.1016/S1003-9953(08)60098-5.

[14] R. Seabra, A. Ribeiro, K. Gleichmann, A. Ferreira, A. Rodrigues, Adsorption equilibrium and kinetics of carbon dioxide, methane and nitrogen on binderless zeolite 4A adsorbents, Micropor. Mesopor. Mat. 277 (2019) 105-114. https://doi.org/10.1016/j.micromeso.2018.10.024.

[15] L. Zhou, X. Liu, L. Li, N. Wang, Z. Wang, Y. Zhou, Synthesis of ordered mesoporous carbon molecular sieve and its adsorption capacity for H2, N2, O2, CH4 and CO2, Chem. Phys. Lett. 41 (2005) 6-9. https://doi.org/10.1016/j.cplett.2005.07.048.

[16] D. Qu, Y. Yang, K. Lu, L. Yang, P. Li, J. Yu, A. Ribeiro, A. Rodrigues, Microstructure effect of carbon materials on the low-concentration methane adsorption separation from its mixture with nitrogen, Adsorption 24 (2018) 357-369. https://doi.org/10.1007/s10450-018-9951-4.

[17] B. Wang, L-H. Xie, X. Wang, X-M. Liu, J. Li, J-R. Li, Applications of metal-organic frameworks for green energy and environment: New advances in adsorptive gas separation, storage and removal, Green Energy Environ. 3 (2018) 191-228. https://doi.org/10.1016/j.gee.2018.03.001.

[18] L. Li, L. Yang, J. Wang, Z. Zhang, Q. Yang, Y. Yang Y, Highly efficient separation of methane from nitrogen on a squarate-based metal-organic framework, AlChE J. 64 (2018) 3681-3690. https://doi.org/10.1002/aic.16335.

[19] S. Eyer, N. Stadie, A. Borgschulte, L. Emmenegger, J. Mohn, Methane preconcentration by adsorption: a methodology for materials and conditions selection, Adsorption 20 (2014) 5-6. https://doi.org/10.1007/s10450-014-9609-9.

[20] J. Yang, Y. Wang, L. Li, Z. Zhang, J. Li, Protection of open-metal V(III) sites and their associated CO2/CH4/N2/O2/H2O adsorption properties in mesoporous V-MOFs, J. Colloid Interface. Sci. 456 (2015) 197-205. https://doi.org/10.1016/j.jcis.2015.06.036.

[21] R. Sabouni, H. Kazemian, S. Rohani, Mathematical modeling and experimental breakthrough curves of carbon dioxide adsorption on metal organic framework CPM-5, Environ. Sci. Technol. 47 (2013) 9372-9380. https://doi.org/10.1021/es401276r.

[22] P.G. Aguilera, F.J. Gutiérrez Ortiz, Prediction of fixed-bed breakthrough curves for H2S adsorption from biogas: Importance of axial dispersion for design, Chem. Eng. J. 289 (2016) 93-98. https://doi.org/10.1016/j.cej.2015.12.075.

[23] J. Delgado, M. Uguina, J. Sotelo, B. Ruiz, Modelling of the fixed-bed adsorption of methane/nitrogen mixtures on silicalite pellets, Sep. Purif. Technol. 50 (2006) 192-203. https://doi.org/10.1016/j.seppur.2005.11.026.

[24] B. Babu, S. Gupta, Modeling and simulation of fixed bed adsorption column: Effect of velocity variation, Birla Institute of Technology and Science (2005) https://doi.org/10.26634/jfet.1.1.966.

[25] S. Nouh, K. Lau, A. Shariff, Modeling and simulation of fixed bed adsorption column using integrated CFD approach, J. Appl. Sci. 10 (2010) 3229-3235. https://doi.org/10.3923/jas.2010.3229.3235.

[26] X. Peng, D. Cao, J. Zhao, Grand canonical Monte Carlo simulation of methane-carbon dioxide mixtures on ordered mesoporous carbon CMK-1, Sep. Pur. Tech. 68 (2009) 50-60. https://doi.org/10.1016/j.seppur.2009.04.005.

[27] Q. Yang, C. Zhong, Molecular simulation of carbon dioxide/methane/hydrogen mixture adsorption in metal-organic frameworks, J. Phys. Chem. B 110 (2006) 17776-17783. https://doi.org/10.1021/jp062723w.

[28] Y. Peng, V. Krungleviciute, I. Eryazici, J. Hupp, O. Farha, T. Yildirim, Methane storage in metal-organic frameworks: Current records, surprise findings, and challenges, J. Am. Chem. Soc. 135 (2013) 11887-11894. https://doi.org/10.1021/ja4045289.

[29] M. Sánchez-Sánchez, I. Asua, D. Ruano, K. Díaz, Direct synthesis, structural features, and enhanced catalytic activity of the Basolite F300-like semiamorphous Fe-BTC framework, Cryst. Growth Des. 15 (2015) 4498-4506. https://doi.org/10.1021/acs.cgd.5b00755.

[30] J. Mollmer, M. Lange, A. Moller, C. Patzschke, K. Stein, D. Lassig, J. Lincke, R. Glaser, H. Krautscheid, R. Staudt, Pure and mixed gas adsorption of CH4 and N2 on the metal-organic framework Basolite® A100 and a novel copper-based 1,2,4-triazolyl isophthalate MOF, J. Mater. Chem. 22 (2012) 10274-10286. https://doi.org/10.1039/c2jm15734a.

[31] A. Dhakshinamoorthy, M. Alvaro, P. Horcajada, E. Gibson, M. Vishnuvarthan, A. Vimont, J. Grenèche, C. Serre, M. Daturi, H. García, Comparison of porous iron trimesates Basolite F300 and MIL-100(Fe) as heterogeneous catalysts for Lewis acid and oxidation reactions: Roles of structural defects and stability, ACS Catal. (2012) 2:2060-2065. https://doi.org/10.1021/cs300345b.

[32] C. Perego, S. Peratello, Experimental methods in catalytic kinetics, Catal. Today 14 (1999) 133-145. https://doi.org/10.1016/S0920-5861(99)00071-1.

[33] Z. Niu, X. Cui, T. Pham, P. Lan, H. Xing, K. Forrest, L. Wojtas, B. Space, S. Ma, A metal-organic framework based methane nano-trap for the capture of coal-mine methane, Angewandte Chemie 58 (2019) 10138-10141. https://doi.org/10.1002/anie.201904507.

[34] D. Wu, X. Guo, H. Sun, A. Navrotsky, Thermodinamics of methane adsorption on copper HKUST-1 at low pressure, J. Phys. Chem. Lett. 6 (2015) 2439-2443. https://doi.org/10.1021/acs.jpclett.5b00893.

[35] D. Ursueguía, E. Díaz, S. Ordóñez, Adsorption of methane and nitrogen on Basolite MOFs: equilibrium and kinetic studies, Micropor. Mesopor. Mater. 298 (2020) https://doi.org/10.1016/j.micromeso.2020.110048.

[36] G. Standart, The thermodynamic significance of the Danckwerts' boundary conditions, Chem. Eng. Sci. 23 (1968) 645-655. https://doi.org/10.1016/0009-2509(68)89009-8.

[37] E. Fuller, P. Schettler, J. Giddings, New method for prediction of binary gas-phase diffusion coefficients, Ind. Eng. Chem. 58 (1966) 18-27. https://doi.org/10.1021/ie50677a007.

[38] J. Theuerkauf, P. Witt, D. Schwesig, Analysis of particle porosity distribution in fixed beds using the discrete element method, Powder Technol. 165 (2006) 92-99. https://doi.org/10.1016/j.powtec.2006.03.022.

[39] S. Farooq, H. Qinglin, I. Karimi, Identification of transport mechanism in adsorbent micropores from column dynamics, Ind. Eng. Chem. Res. 41 (2002) 1098-1106. https://doi.org/10.1021/ie0104621.

[40] D. Saha, Z. Bao, F. Jia, S. Deng, Adsorption of CO2, CH4, N2O and N2 on MOF-5, MOF-177, and Zeolite 5A, Environ. Sci. Technol. 44 (2010) 1820-1826. https://doi.org/10.1021/es9032309.

[41] P. Bárcia, L. Bastin, E. Hurtado, J. Silva, A. Rodrigues, B. Chen, Single and multicomponent sorption of CO_2, CH_4 and N_2 in a Microporous Metal-Organic Framework, Sep. Sci. Tech. 43 (2008) 3494-3521. https://doi.org/10.1080/01496390802282347.

[42] Z. Bao, L. Yu, Q. Ren, X. Lu, S. Deng, Adsorption of CO2 and CH4 on a magnesium-based metal organic framework, J. Colloid Interface Sci. 353 (2011) 549-556. https://doi.org/10.1016/j.jcis.2010.09.065.

[43] B. Panella, M. Hirscher, S. Roth, Hydrogen adsorption in different carbon nanostructures, Carbon 43 (2005) 2209-2214. https://doi.org/10.1016/j.carbon.2005.03.037.

[44] H. Frost, T. Duren, R. Snurr, Effects of surface area, free volume, and heat of adsorption on hydrogen uptake in metal-organic frameworks, J. Phys. Chem. B 110 (2006) 9565-9570. https://doi.org/10.1021/jp060433.

[45] A. Mukhtar, N. Mellon, S. Saqib, A. Khawar, S. Raqif, S. Ullah, A. Al-Sehemi, M. Babar, M. Bustam, W. Khan, M. Tahir, CO2/CH4 adsorption over functionalized multi-walled carbon nanotubes; an experimental study, isotherms analysis, mechanism, and thermodynamics, Micropor. Mesopor. Mat. 294 (2020) 109883. https://doi.org/10.1016/j.micromeso.2019.109883.

[46] A. Lyubchyk, I. Esteves, F. Cruz, J. Mota, Experimental and theoretical studies of supercritical methane adsorption in the MIL-53(Al) metal organic framework, J. Phys. Chem. C 115 (2011) 20628-20638. https://doi.org/10.1021/jp207326d.

[47] F. Lovas, R. Suenram, J. Coursey, S. Kotochigova, J. Chang, K. Olsen, R. Dragoset, Hydrocarbon spectral database, NIST standard reference database 115 (2004). https://dx.doi.org/10.18434/T4PC70.

[48] S. Couck, J. Denayer, G. Baron, T. Remy, J. Gascon, F. Kapteijn, An amine-functionalized MIL-53 metal-organic framework with large separation power for CO2 and CH4, J. Am. Chem. Soc. 131 (2009) 6326-6327. https://doi.org/10.1021/ja900555r.

[49] E. Deniz, F. Karadas, H. Patel, S. Aparicio, C. Yavuz, M. Atilhan, A combined computational and experimental study of high pressure and supercritical CO2 adsorption on Basolite MOFs, Micropor. Mesopor. Mat. 175 (2013) 34-42. http://dx.doi.org/10.1016/j.micromeso.2013.03.015.

[50] Z. Li, G. Xiao, Q. Yang, Y. Xiao, C. Zhong, Computational exploration of metal-organic frameworks for CO2/CH4 separation via temperature swing adsorption, Chem. Eng. Sci. 120 (2014) 59-66. http://dx.doi.org/10.1016/j.ces.2014.08.003.

[51] Z. Zhao, X. Li, Z. Li, Adsorption equilibrium and kinetics of p-xylene on chromium-based metal organic framework MIL-101, Chem. Eng. J. 173 (2011) 150-157. https://doi.org/10.1016/j.cej.2011.07.051.

[52] L. Arnold, G. Averlant, S. Marx, M. Weickert, U. Muller, J. Mertel, C. Horch, M. Peksa, F. Stallmach, Metal Organic Frameworks for natural gas storage in vehicles, Chem. Ing. Tech. 11 (2013) 1726-1733. https://doi.org/10.1002/cite.201300093.

[53] R. Hernández-Huesca, L. Díaz, G. Aguilar-Armenta, Adsorption equilibria and kinetics of CO2, CH4 and N2 in natural zeolites, Sep. Pur. Tech. 15 (1999) 163-173. https://doi.org/10.1016/S1383-5866(98)00094-X.

[54] G. Walker, L. Weatherley, Adsorption of acid dyes on to granular activated carbon in fixed beds, Wat. Res. 31 (1997) 2093-2101. https://doi.org/10.1016/S0043-1354(97)00039-0.

[55] H. Patel, Fixed-bed column adsorption study: a comprehensive review, Appl. Water Sci. 9 (2019) 45. https://doi.org/10.1007/s13201-019-0927-7.

[56] E. Malkoc, Y. Nuhoglu, Y. Abali, Cr(VI) adsorption by waste acorn of Quercus Ithaburensis in fixed beds: Prediction of breakthrough curves, Chem. Eng. J. 119 (2006) 61-68. https://doi.org/10.1016/j.cej.2006.01.019.

[57] N. Abdel-Jabbar, S. Al-Asheh, B. Hader, Modeling, parametric estimation, and sensitivity analysis for copper adsorption with moss packed-bed, Sep. Sci. Technol. 36 (2001) 2811-2833. http://dx.doi.org/10.1081/SS-100107631.

LIST OF SYMBOLS AND ABBREVIATIONS

BASF	Badische Anilin- und Soda-Fabrik
MOFs	Metal-Organic Frameworks
VAM	Ventilation Air Methane
US	United States
TSA	Temperature Swing Adsorption
GCMC	Gran-Canonical Monte Carlo
LDF	Linear Driving Force
MUMPS	Multifrontal Massively Parallel sparse direct Solver
D	Bed diameter (m)
d_p	Particle diameter (m)
L	Bed length (m)
C_i	Methane concentration in gas phase (mol/m^3)
t	Time (s)
u_0	Surface velocity (m/s)
ε_b	Bed porosity (-)
z	Bed axial position (m)
D_e	Axial dispersion (m^2/s)
ρ_b	Bed density (kg/m^3)
q_i	Methane concentration in solid phase (mol/kg)
W_i	Methane concentration in solid phase (mol/kg)
K_{Hi}	Henry isotherm constant (m^3/kg)
W_{ieq}	Solid-gas equilibrium concentration (mol/kg)
Q_{mi}	Maximum capacity (Langmuir model) (mol/kg)
K_{Li}	Langmuir isotherm constant (mol/m^3)
L_b	Axial position at the end of fixed bed (m)
Pe	Péclet number (-)
D_m	Molecular diffusion (m^2/s)
T	Temperature (K)
M_i	Molecular mass of component i (g/mol)
P	Total pressure (Pa)
V_i	Diffusion volume (-)
k_L	Global mass transfer coefficient (1/s)
k_f	Film mass transfer coefficient (1/s)
r_p	Crystal radius (m)

ε_p	Particle porosity (-)
D_p	Macropore diffusivity (m^2/s)
D_i	Micropore diffusivity (m^2/s)
$C_{max,CH4}$	Maximum concentration of methane at the outlet of desorption (%)